



Self-Pillared Ultramicroporous Carbon Nanoplates for Selective Separation of CH₄/N₂

Shuang Xu, Wen-Cui Li, Cheng-Tong Wang, Lei Tang, Guang-Ping Hao,* and An-Hui Lu*

Abstract: There is growing evidence that pillaring up a densely packed ultramicroporous two-dimensional (2D) structure is an effective strategy to reduce their internal diffusion. Reliable pillaring paradigms, however, is rather challenging. Here we report a one-pot multi-component sequential assembly method for the preparation of a new self-pillared 2D polymer and ultramicroporous carbon with integrated surface protrusions. The molecular level pillaring process is surprisingly fast, that is, in 10 min. The thickness of nanoplate edge and the density (roughness), angle as well as height of protrusions can be precisely tuned. Exemplified in coal bed methane purification/separation, this unique pillared 2D carbons exhibit a CH₄/N₂ selectivity up to 24 at a low CH₄ partial pressure and two orders of magnitude faster CH₄ diffusion kinetics than the commercial carbon molecular sieves. This solution synthesis methodology is generalizable for creation and fine tuning of pillared 2D heterostructures.

Coal bed methane, a kind of paramount unconventional natural gas, is composed of the fuel component CH₄ and the predominant impurity of N₂. For its efficient utilization, separating CH₄ from the gas mixture is required.^[1,2] However, the very close molecular size and similar polarity of N₂ and CH₄ make their separation critically difficult, where a precisely controlled ultra-micropore (< 7 Å) is the indispensable prerequisite.^[3] Unfortunately, for pores at such a length scale, the long-lasting and ubiquitous challenge is their markedly increased mass-transport limitations due to long diffusion paths and narrow apertures,^[4] resulting in reduced efficiency of the process.^[5]

Porous carbon materials that possess highly developed porosity and excellent stability are widely explored as adsorbents for selective CH₄/N₂ separation.^[6] The main separation mechanisms include targeted CH₄ or N₂ recognition, equilibrium or kinetic selectivity. For either way, a rapid molecular transport is favored for an efficient CH₄ purification or separation from N₂. However, the amorphous carbonaceous bulky materials with rich ultramicropores display sluggish internal diffusion due to their intrinsic

turbostratic structures. To alleviate this issue, the most straightforward way is to enhance transport kinetics by imparting hierarchical porosity.^[7] For instance, a series of synthesis strategies, including templating, self-assembly, were exploited for the creation of the interconnected multi-scale macro- to micro-pores.^[8] Alternatively, downsizing their dimension is another way to enhance the transport kinetics.^[9] For example, porous 2D nanocarbons were prepared, where mono-/few layer graphene oxide or other 2D templates were served as shape-directing agents.^[10] Similarly, 2D carbon nanostructures were fabricated by the surface-assisted method on metals surface or air–water interface.^[11] These strategies, to a large extent, addressed the diffusion limitation issue, however, the CH₄/N₂ selectivity on carbonaceous adsorbent is still unsatisfied in their practical separation.^[12] To enable a sweet spot of kinetics and thermodynamics for CH₄/N₂ effective separation, we envisage that pillaring up the 2D carbons with dense ultramicropores by nano-protrusions would further boost the selective separation of CH₄/N₂. However, the research on self-pillared 2D nanocarbon is still very nascent. The challenging task requires not only a well-controlled growth of the nanopillars but also a matched self-assembly for the spatially selective anchoring of nanopillars on the targeted sites.^[13] Unfortunately, the method for synthesis of pillared 2D structure in solution phase is still missing.

Taking up this challenge, herein, we report a one-pot self-pillaring method to intensify the diffusion kinetics via a highly processable solution synthesis strategy. The synthesis of pillared polymer nanoplates (PPNPs) is based on a multi-component sequential assembly, in which the protrusions of the PPNPs were in situ grown on the soft 2D templates through the nucleophilic attack induced sequential condensation of phloroglucinol (POL), terephthalaldehyde (TPA) and *p*-phenylenediamine (*p*-PDA) (Figure 1a). The soft templates were formed by the self-assembly of triblock copolymers and stearic acid, to which the POL and TPA were first introduced. Then, the rapid condensation reaction was initiated by *p*-PDA and proceeded very fast (in 10 min) in solution towards the formation of such pillared heterostructure. The time-resolved structural evolution was recorded by SEM, confirmed the rapid growing and assembly process (Supporting Information, Figure S1). The results show that the nucleation was spatially selective, which took place preferentially at higher energy sites, including the whole edges and the defective sites on the basal plane. The corresponding polymerization reactions for the formation of the PPNPs are shown in Figure 1b.

To further disclose the key factors influencing the formation of the unique heterostructure, a series of control

[*] S. Xu, Prof. W. C. Li, C. T. Wang, L. Tang, Prof. G. P. Hao, Prof. A. H. Lu

State Key Laboratory of Fine Chemicals, Liaoning Key Laboratory for Catalytic Conversion of Carbon Resources, and School of Chemical Engineering, Dalian University of Technology
Dalian 116024 (P. R. China)
E-mail: guangpinghao@dlut.edu.cn
anhuilu@dlut.edu.cn

Supporting information and the ORCID identification number(s) for the author(s) of this article can be found under:
<https://doi.org/10.1002/anie.202014231>.

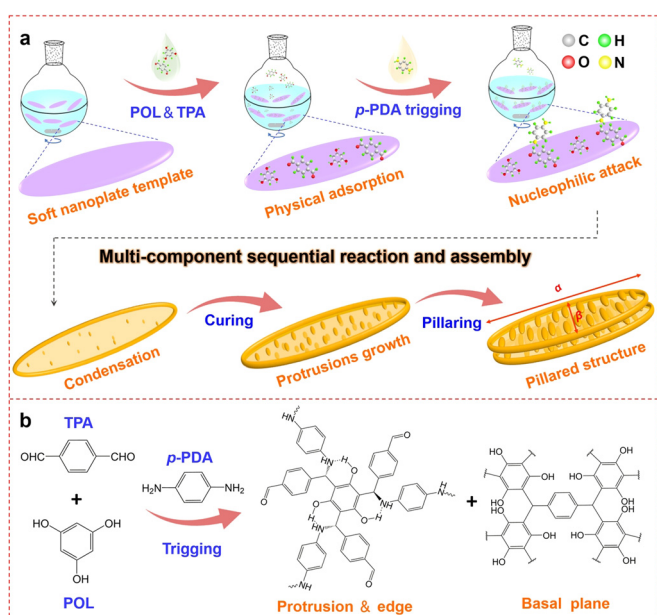


Figure 1. a) The synthesis based on *p*-PDA triggered condensation of POL, TPA, and *p*-PDA. b) The corresponding polymerization reactions for the formation of the pillared 2D structures.

experiments were conducted (Supporting Information, Figure S2). A much faster reaction was found between TPA and *p*-PDA (completed in 3 min) than that of TPA and POL (started after about 30 min; Supporting Information, Figure S2a). In the absence of *p*-PDA, the phenolic condensation of TPA and POL on the soft 2D templates (TPOL) led to the formation of similar nanoplate but showing a smooth surface (Supporting Information, Figure S2b). While the Schiff base reaction of TPA and *p*-PDA on the soft 2D templates (TPDA) resulted in the generation of polymeric rings (Supporting Information, Figure S2c). These phenomena indicate the preferential polymerization between *p*-PDA and TPA at the edge sites owing to the highly reactive nucleophilic addition of an amine to a carbonyl group. When the polymerization of POL, TPA and *p*-PDA took place on the soft 2D templates, the special PPNPs could be prepared successfully.

The formation process of the pillared structures was monitored by the ex-situ solid NMR and FTIR spectra (Supporting Information, Figure S3). As shown in ^{13}C CP/MAS NMR spectra, the carbon signal at around 156 ppm in TPDA belongs to the C=N bond of Schiff base.^[14] The slightly shifted band also appears in the PPNPs but with higher intensity due to the overlapping with the phenoxy carbon (Supporting Information, Figure S3a). The FTIR analyses show an adsorption band at 1612 cm^{-1} , which can be assigned to the C=N stretching vibrations, and the peak at about 1220 cm^{-1} is N-C stretching band. Moreover, the band at 3200 cm^{-1} become stronger with the increased *c*(*p*-PDA), which confirms the formation of polymer frameworks through the co-condensation of TPA, POL and *p*-PDA (Supporting Information, Figure S3b).^[15] As described and discussed above, we believe the key for the formation of the PPNPs lies in the precisely match of the reaction rates between the phenolic

condensation and the *p*-PDA initiated Mannich reaction and polymerization (Figure 1b).

Furthermore, the resultant PPNPs show uniformly elliptical shape with a semi-major (α) and semi-minor (β) axis of 5–7 and 1.0–1.3 μm , respectively (Figure 2a; Supporting Information, Figure S4a,b). The protrusions also exhibit similarly elliptical shape, but with one order of magnitude smaller size. The areal density of the protrusions is estimated to be $2.2 \times 10^8\text{ cm}^{-2}$. More quantitatively, the average height of the protrusions on the basal plane is $31.4 \pm 4.9\text{ nm}$, which is roughly at the same level as the orbit edge (Figure 2c). Upon thermal treatment at 800°C , the PPNPs were transformed into their shrunk carbonaceous counterparts (PCNPs), while the morphology was well maintained. The elliptical protrusions with an average height of 8 nm grow perpendicularly and anchor tightly on the elliptical basal plane (Figure 2d), forming a pillared surface heterostructure and the basal plane of about 6 nm (Figure 2d, inset). Such pillared structures lead to a roughness factor of 36.7 ± 3.8 for PCNPs. Notably, because of the pillared structure, the PCNPs sample shows a lower packing density (0.117 g cm^{-3}) than its tightly packed smooth counterpart (0.135 g cm^{-3}). Furthermore, the CO_2 and N_2 physisorption analyses reveal that the ultramicropore at around 4.8 Å is predominated, contributing 65% of the total micropore volume (Figure 2b; Supporting Information, Fig-

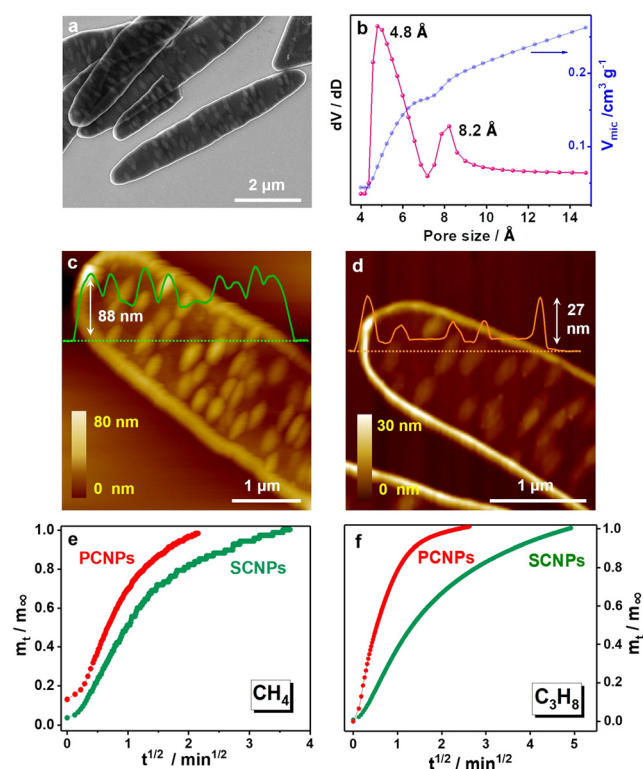


Figure 2. a) SEM image of polymer nanoplates with nanopillars. b) Micropore size distribution and micropore volume determined from CO_2 adsorption at 273 K. c,d) AFM images of PPNPs (*c*(*p*-PDA) is 0.33 M) and PCNPs and corresponding cross-section analysis for the dashed green and orange line in the images. e),f) The comparison of kinetic adsorption of CH_4 and C_3H_8 for PCNPs and SCNPs at 20 mbar and 25 mbar (298 K), respectively.

ure S5). The rich micropores enable a high specific surface area, reaching up to $690 \text{ m}^2 \text{ g}^{-1}$.

High accessibility to the adsorption sites would facilitate a fast mass transfer, thus a feasible short cycle time for pressure swing adsorption process. From this perspective, our PCNPs with patterned nanopillars and 6 nm thin 2D basal planes could be the ideal model for the reduction of the internal diffusion. Thus, we examined the adsorption kinetics of CH_4 (3.8 Å) and C_3H_8 (5.1 Å) on PCNPs and the contrast sample smooth SCNPs with similar pore distribution (Figure 2 e,f; Supporting Information, Figure S5c,d). For CH_4 , the PCNPs show the highest diffusion time constants (D/r^2) up to $1.18 \times 10^{-3} \text{ s}^{-1}$ which is 2.3 times higher than their smooth counterparts, SCNPs ($5.06 \times 10^{-4} \text{ s}^{-1}$), and two orders of magnitude higher than the commercial CMS (Takeda 3kt, $D/r^2 = 1.19 \times 10^{-5} \text{ s}^{-1}$, Bergbau-Forschung BF-1.0, $4.26 \times 10^{-6} \text{ s}^{-1}$, Table S1).^[16a, 19b] For larger C_3H_8 probe, a similar trend is observed (Figure 2 f). On PCNPs, it reaches adsorption equilibrium within 6 min, which is much faster than that of SCNPs (20 min). The results verify the notable advantages for faster diffusion kinetics enabled by such pillared heterostructures, which greatly outperform the dense 2D structures and other three-dimensional porous carbons.

We further verified the tuning flexibility of the novel structure of PPNPs. Not only the areal density but also the height of the protrusions can be regulated continuously by varying the concentration of *p*-PDA, $c(p\text{-PDA})$. With increasing of $c(p\text{-PDA})$ from 0.04 to 0.5 M, the areal densities of the protrusions increased 67 times, with a value of around $0.04 \times 10^8 \text{ cm}^{-2}$ to $2.7 \times 10^8 \text{ cm}^{-2}$, respectively (Figure 3 a–d). Such

a phenomenon can be interpreted as that with the higher content of *p*-PDA, the amount of imine intermediate generated by *p*-PDA and TPA increases, resulting in more nucleation sites. Consequently, the protrusions grow gradually around the initial nucleation sites. This is also proved by the solid NMR and FTIR spectra (Supporting Information, Figure S3). From Figure 3 e, the edge height can be tailored, spanning from 30 to 120 nm. Interestingly, the same trends are also observed on surface roughness, which increases linearly as increasing $c(p\text{-PDA})$ (Figure 3 e; Supporting Information, Table S2). It indicates that the edge sites are intrinsically as reactive as that for the growth of the protrusions on the basal plane. Besides the protrusions and edges, the thickness changes of the basal plane (Figure 3 f) are recorded, which can be adjusted from 20–40 nm. By calculating the slopes, the growth rates can be extracted, which is 57.3, 120, and 42.4 nm/M *p*-PDA, for protrusions, edges, and basal planes, respectively. The former two display a fast growth rate, which is 1.5 and 2.8 times higher than that of basal planes. This reflects the difference in reactivity and confirms the active sites-oriented growth mechanism of the PPNPs. Furthermore, the STEM mapping and the N1s XPS of the PCNPs together indicate the difference in composition between the basal plane and the protrusions, and further disclose the formation mechanism of the PPNPs (Supporting Information, Figures S6, S7 and Table S3).

Surprisingly, for protrusions, not only the height can be tuned but also their direction, perpendicular or parallel to the basal plane. Under dynamic conditions (stirring), the protrusions are arranged orderly on the surface perpendicular to the major axis of the basal plane (Figure 3 g). On the contrary, the protrusions arrange more parallel to the basal plane under static conditions (Figure 3 h). We speculate that the intermediate phase of the protrusions remains metastable, which could be nanoengineered by shearing force.

Figure 4 a displays the adsorption isotherms, which reveal an uptake of 1.17 and 0.28 mmol g^{-1} at 298 K and 1 bar for CH_4 and N_2 , respectively. The isosteric adsorption heats (Q_{st}) of CH_4 and N_2 on PCNPs were calculated (Supporting Information, Figure S8a). The CH_4 adsorption heat of 22.3 kJ mol^{-1} is visibly lower than the typical benchmarks of Na-ZSM-5 (26.5 kJ mol^{-1}),^[16b] Na mordenite ($24\text{--}25 \text{ kJ mol}^{-1}$),^[16c] Mg-MOF-74 (26.3 kJ mol^{-1}),^[16d] $\text{Cu}_2(\text{ATC})$ (26.8 kJ mol^{-1}),^[2a] $\text{Co}_3(\text{C}_4\text{O}_4)_2(\text{OH})_2$ ($25.13 \text{ kJ mol}^{-1}$),^[16e] $\text{CuB}_{12}\text{H}_{12}(\text{bpa})_2$ (23.7 kJ mol^{-1}).^[16f] The moderate Q_{st} of CH_4 enables an easy regeneration under mild conditions. The ideal selectivity of CH_4/N_2 mixtures was calculated based on the ideal adsorbed solution theory (IAST, Figure 4 b). The isotherms were fitted based on the single-site Langmuir-Freundlich equation (Supporting Information, Table S4). IAST selectivities remain steady with a decrease of the gas phase mole fraction of CH_4 (Figure 4 b above). For CH_4/N_2 (v/v 30/70), the selectivity was calculated to be around 10 at 298 K 1 bar. Importantly, the low-pressure selectivity (below 0.1 bar) is up to 24 (Figure 4 b below), indicating the potential for separation of low-concentration methane. The detailed comparison of CH_4 uptake capacity and selectivity were summarized in Figure 4 c and the Supporting Information, Table S5. The CH_4/N_2 selectivity is in the leading position, and

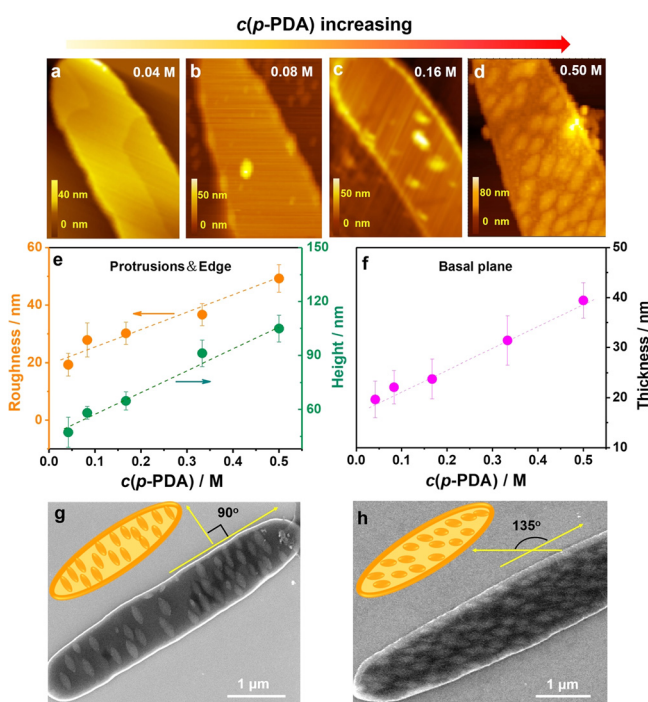


Figure 3. AFM images of PPNPs synthesized with different molar concentration of *p*-PDA: a) 0.04 M, b) 0.08 M, c) 0.16 M, d) 0.50 M. e), f) the relationships between $c(p\text{-PDA})$ and roughness, height of orbit edges of PPNPs and thickness of basal plane. g), h) SEM images of PPNPs at (g) dynamic and (h) static conditions.

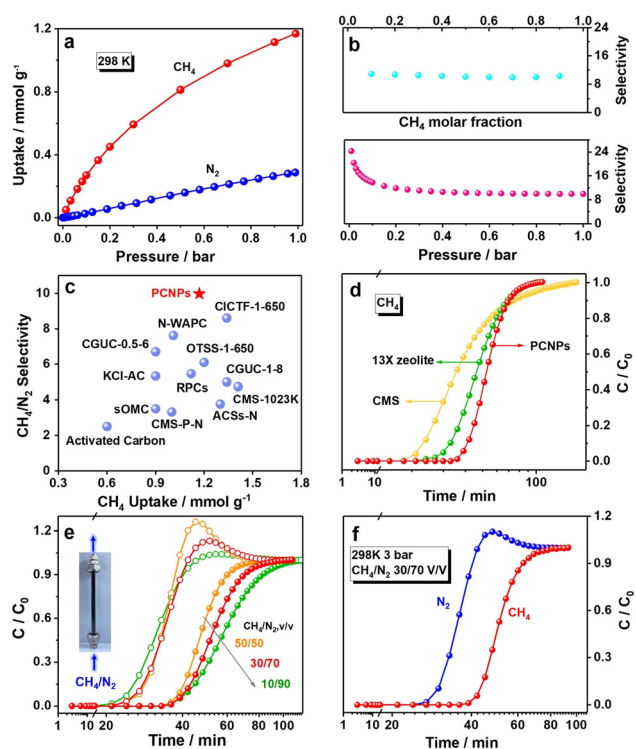


Figure 4. a) CH_4 and N_2 adsorption isotherms. b) IAST selectivity of PCNPs as a function of CH_4 molar fraction of mixtures of CH_4/N_2 (above) and of pressure for mixtures of CH_4/N_2 (30/70 v/v) at 298 K (below). c) Comparison of selectivity and CH_4 adsorption capacity on PCNPs and other benchmarks. Breakthrough curves of PCNPs for CH_4 (d) and CH_4/N_2 with varied compositions (e) at 298 K and 1.0 bar. (f) Breakthrough curves of PCNPs for CH_4/N_2 (30:70 v/v) mixtures at 298 K and 3.0 bar.

the CH_4 adsorption capacity is comparable to the state-of-the-art carbon adsorbents. For instance, the CH_4/N_2 selectivity of PCNPs is 3–10 times higher than commercial activated carbon and zeolites (5A, 13X);^[17,18] PCNPs exhibit 2.7 and 2.0 times higher CH_4/N_2 selectivity compared with N-doped porous carbon (ACSS-N) and carbon molecular sieve (CMS-1023 K),^[19] while the CH_4 adsorption capacity is comparable.

For the evaluation of adsorption kinetics, the single-component CH_4 breakthrough kinetics of the packed column of the PCNPs were further compared (Figure 4d). In the mass-transfer zone between the breakthrough point and saturation, the adsorption of PCNPs rapidly reaches the equilibrium state with a sharper slope than that of the CMS and zeolite 13X, confirming the rapid gas diffusion and enhanced mass transfer in the pillared microporous PCNPs. This trend is consistent with the time-resolved gravimetric results as shown in Figure 2e,f. The dynamical breakthrough experiments for mixtures of CH_4/N_2 (10:90, 30:70 and 50:50 v/v) were performed (Figure 4e). First, the N_2 eluted from the packed bed quickly, 15–18 min later CH_4 penetrate. A notable roll-up effect is observed along the elution of N_2 for gas mixtures with CH_4 concentration higher than 30%. This is indicative of the pre-adsorption of N_2 , which is replaced by the preferential CH_4 on the adsorption sites. When the concentration of eluting gas reaches a constant value, the adsorption capacity of CH_4 on the column is 0.81 mmol g^{-1} ,

being 3.5 times higher than that of N_2 . This proves the impressive efficiency of PCNPs for actual CH_4/N_2 adsorption separation.

To mimic the realistic coal bed methane conditions, the separation of CH_4/N_2 at higher pressure (3–20 bar) was investigated through a PSA cycle (Figure 4f; Supporting Information, Figure S8b). The PCNPs is still capable of effectively separating CH_4 from N_2 with a selectivity up to 6 and 5 at 3 and 20 bar, respectively. This remarkable adsorption separation performance is ascribed to collaborating features in terms of the narrow ultramicropore size distribution (4.8 Å) and the highly accessible transport pathways. Moreover, the regeneration ability of the PCNPs had been examined (Supporting Information, Figure S8c,d), where a vacuum regeneration was employed. The adsorption capacity remained higher than 98% even after 10 successive adsorption-desorption cycles. Importantly, the PCNPs can also exhibit excellent dynamic adsorption-separation of CH_4/N_2 under elevated temperature (308 K) and at ternary mixture of $\text{CH}_4/\text{N}_2/\text{O}_2$ ($\text{CH}_4/\text{N}_2/\text{O}_2$, v/v/v 30:53.3:16.7) with a selectivity higher than 3, which indicates the potential for a realistic application (Supporting Information, Figure S8e,f).

In conclusion, a self-pillaring solution synthesis strategy is demonstrated, which enables the creation of a unique class of 2D polymers and ultramicroporous carbons with integrated surface protrusions. The molecular level pillaring process is facile and fast through multi-component sequential polymerization. The core structural parameters in terms of protrusions density, angles and height of edges can be precisely tailored. When applied as adsorbents for CH_4/N_2 separation, the pillared ultramicroporous carbons show a highly competitive CH_4/N_2 selectivity at lower CH_4 partial pressure, a rapid CH_4 diffusion and the excellent cycle stability. This multi-component sequential assembly strategy is effective for fine manipulation of pillared 2D structures, and potentially applicable to other 2D heterostructures.

Acknowledgements

The research was financially supported by the National Natural Science Foundation for Distinguished Young Scholars (No. 21225312), the Cheung Kong Scholars Program of China (T2015036), and the Fundamental Research Funds for the Central Universities(DUT20GJ215).

Conflict of interest

The authors declare no conflict of interest.

Keywords: carbon nanoplates · CH_4/N_2 separation · hierarchical structures · porous carbon nanomaterials · self-assembly

[1] a) H. Shang, Y. P. Li, J. Q. Liu, X. Tang, J. F. Yang, J. P. Li, *Chin. J. Chem. Eng.* **2019**, *27*, 1044–1049; b) R. L. Tang, Q. B. Dai, W. W. Liang, Y. Wu, X. Zhou, H. Y. Pan, Z. Li, *Chem. Eng. J.*

- 2020, 384, 123388; c) Y. Q. Wu, D. H. Yuan, D. W. He, J. C. Xing, S. Zeng, S. T. Xu, Y. P. Xu, Z. M. Liu, *Angew. Chem. Int. Ed.* **2019**, 58, 10241–10244; *Angew. Chem.* **2019**, 131, 10347–10350.
- [2] a) Z. Niu, X. L. Cui, T. Pham, P. C. Lan, H. B. Xing, K. A. Forrest, L. Wojtas, B. Space, S. Q. Ma, *Angew. Chem. Int. Ed.* **2019**, 58, 10138–10141; *Angew. Chem.* **2019**, 131, 10244–10247; b) S. J. Du, Y. Wu, X. J. Wang, Q. B. Xia, J. Xiao, X. Zhou, Z. Li, *AIChE J.* **2020**, 66, 16231.
- [3] a) Z. B. Bao, G. G. Chang, H. B. Xing, R. Krishna, Q. L. Ren, B. L. Chen, *Energy Environ. Sci.* **2016**, 9, 3612–3641; b) M. Oschatz, M. Antonietti, *Energy Environ. Sci.* **2018**, 11, 57–70; c) A. Altwala, R. Mokaya, *Energy Environ. Sci.* **2020**, 13, 2967–2978.
- [4] a) J. Pérez-Ramírez, C. H. Christensen, K. Egeblad, C. H. Christensen, J. C. Groen, *Chem. Soc. Rev.* **2008**, 37, 2530–2542; b) M. A. Sadeghi, M. Aghighi, J. Barralet, J. T. Gostick, *Chem. Eng. J.* **2017**, 330, 1002–1011.
- [5] M. G. Sausen, F. B. Scheufele, H. J. Alves, M. G. A. Vieira, M. G. C. D. Silva, F. H. Borba, C. E. Borba, *Sep. Purif. Technol.* **2018**, 207, 477–488.
- [6] a) Y. Yang, A. M. Ribeiro, P. Li, J.-G. Yu, A. E. Rodrigues, *Ind. Eng. Chem. Res.* **2014**, 53, 16840–16850; b) Y. Zhang, L. Liu, P. X. Zhang, J. Wang, M. Xu, Q. Deng, Z. L. Zeng, S. G. Deng, *Chem. Eng. J.* **2019**, 355, 309–319.
- [7] a) K. Lan, Y. Liu, W. Zhang, Y. Liu, A. Elzatahry, R. C. Wang, Y. Y. Xia, D. Al-Dhayan, N. F. Zheng, D. Y. Zhao, *J. Am. Chem. Soc.* **2018**, 140, 4135–4143; b) P. P. Qiu, B. Ma, C.-T. Hung, W. Li, D. Y. Zhao, *Acc. Chem. Res.* **2019**, 52, 2928–2938; c) C. Prehal, S. Gratz, B. Krüner, M. Thommes, L. Borchardt, V. Presser, O. Paris, *Carbon* **2019**, 152, 416–423.
- [8] a) S. Dutta, A. Bhaumik, K. C.-W. Wu, *Energy Environ. Sci.* **2014**, 7, 3574–3592; b) M. Perovic, S. S. Aloni, Y. Mastai, M. Oschatz, *Carbon* **2020**, 170, 550–557; c) D. D. Han, Y. C. Jiao, W. Q. Han, G. H. Wu, T. T. Li, D. Yang, A. G. Dong, *Carbon* **2018**, 140, 265–275.
- [9] M. Y. Jeon, D. H. Kim, P. Kumar, P. S. Lee, N. Rangnekar, P. Bai, M. Shete, B. Elyassi, H. S. Lee, K. Narasimharao, S. N. Basahel, S. Al-Thabaiti, W. Q. Xu, H. J. Cho, E. O. Fetisov, R. Thyagarajan, R. F. DeJaco, W. Fan, K. A. Mkhoyan, J. I. Siepmann, M. Tsapatsis, *Nature* **2017**, 543, 690–694.
- [10] a) Y. Choi, S. Kim, Y. Choi, J. Song, T.-H. Kwon, O.-H. Kwon, B.-S. Kim, *Adv. Mater.* **2017**, 29, 1701075; b) L.-P. Guo, W.-C. Li, B. Qiu, Z.-X. Ren, J. Du, A.-H. Lu, *J. Mater. Chem. A* **2019**, 7, 5402–5408; c) G.-P. Hao, Z.-Y. Jin, Q. Sun, X.-Q. Zhang, J.-T. Zhang, A.-H. Lu, *Energy Environ. Sci.* **2013**, 6, 3740–3747.
- [11] a) T. Mori, H. Tanaka, A. Dalui, N. Mitoma, K. Suzuki, M. Matsumoto, N. Aggarwal, A. Patnaik, S. Acharya, L. Kumar Shrestha, H. Sakamoto, K. Itami, K. Ariga, *Angew. Chem. Int. Ed.* **2018**, 57, 9679–9683; *Angew. Chem.* **2018**, 130, 9827–9831; b) S. Kim, M. Ju, J. Lee, J. Hwang, J. Lee, *J. Am. Chem. Soc.* **2020**, 142, 9250–9257.
- [12] a) F. Liu, Y. Zhang, P. X. Zhang, M. Xu, T. Tan, J. Wang, Q. Deng, L. Y. Zhang, Y. Q. Wan, S. G. Deng, *Chem. Eng. J.* **2020**, 399, 125812; b) Z. Y. Yang, D. C. Wang, Z. Y. Meng, Y. Y. Li, *Sep. Purif. Technol.* **2019**, 218, 130–137.
- [13] a) K. S. Novoselov, D. Jiang, F. Schedin, T. J. Booth, V. V. Khotkevich, S. V. Morozov, A. K. Geim, *Proc. Natl. Acad. Sci. USA* **2005**, 102, 10451–10453; b) J. Sakamoto, J. V. Heijst, O. Lukin, A. D. Schlüter, *Angew. Chem. Int. Ed.* **2009**, 48, 1030–1069; *Angew. Chem.* **2009**, 121, 1048–1089; c) Q. T. Zhang, Z. L. Zhang, J. Yin, *Adv. Mater. Interfaces* **2019**, 6, 1900561; d) T. Wang, F. Okejiri, Z.-A. Qiao, S. Dai, *Adv. Mater.* **2020**, 32, 2002475.
- [14] G. Y. Li, B. Zhang, J. Yan, Z. G. Wang, *J. Mater. Chem. A* **2014**, 2, 18881–18888.
- [15] J. M. Zhao, M. R. H. S. Gilani, Z. Y. Liu, R. Luque, G. B. Xu, *Polym. Chem.* **2018**, 9, 4324–4331.
- [16] a) X. Yang, Z. Y. Li, C. Z. Zhang, H. Y. Wang, E. L. Zhang, Y. Xing, P. Xiao, R. T. Yang, Y. S. Liu, P. A. Webley, *Chem. Eng. J.* **2019**, 367, 295–303; b) J. A. Dunne, M. Rao, S. Sircar, R. J. Gorte, A. L. Myers, *Langmuir* **1996**, 12, 5896–5904; c) M. D. Macedonia, D. D. Moore, E. J. Maginn, *Langmuir* **2000**, 16, 3823–3834; d) M. K. Rana, H. S. Koh, H. Zuberi, D. J. Siegel, *J. Phys. Chem. C* **2014**, 118, 2929–2942; e) L. Y. Li, L. F. Yang, J. W. Wang, Z. G. Zhang, Q. W. Yang, Y. W. Yang, Q. L. Ren, Z. B. Bao, *AIChE J.* **2018**, 64, 3681; f) Y. B. Zhang, L. F. Yang, L. Y. Wang, S. Duttwyler, H. B. Xing, *Angew. Chem. Int. Ed.* **2019**, 58, 8145–8150; *Angew. Chem.* **2019**, 131, 8229–8234.
- [17] a) D. F. Quinn, *Carbon* **2002**, 40, 2767–2773; b) J. A. C. Silva, A. Ferreira, P. A. P. Mendes, A. F. Cunha, K. Gleichmann, A. E. Rodrigues, *Ind. Eng. Chem. Res.* **2015**, 54, 6390–6399; c) M. Mofarahi, A. Bakhtyari, *J. Chem. Eng. Data* **2015**, 60, 683–696.
- [18] H. Y. Pan, Y. Yi, Q. Lin, G. Y. Xiang, Y. Zhang, F. Liu, *J. Chem. Eng. Data* **2016**, 61, 2120–2127.
- [19] a) Y. Li, S. Y. Wang, B. B. Wang, Y. Wang, J. P. Wei, *Nanomaterials* **2020**, 10, 174; b) J. H. Zhang, S. J. Qu, L. T. Li, P. Wang, X. F. Li, Y. F. Che, X. L. Li, *J. Chem. Eng. Data* **2018**, 63, 1737–1744.

Manuscript received: October 23, 2020

Revised manuscript received: December 4, 2020

Accepted manuscript online: December 16, 2020

Version of record online: February 2, 2021